



CHORUS

This is the accepted manuscript made available via CHORUS. The article has been published as:

## Three-Dimensional Measurement of the Helicity-Dependent Forces on a Mie Particle

Lulu Liu, Andrea Di Donato, Vincent Ginis, Simon Kheifets, Arman Amirzhan, and Federico Capasso

Phys. Rev. Lett. **120**, 223901 — Published 31 May 2018

DOI: [10.1103/PhysRevLett.120.223901](https://doi.org/10.1103/PhysRevLett.120.223901)

# Three-Dimensional Measurement of the Helicity-Dependent Forces on a Mie Particle

Lulu Liu,<sup>1</sup> Andrea Di Donato,<sup>1,2</sup> Vincent Ginis,<sup>1,3,\*</sup> Simon Kheifets,<sup>1</sup> Arman Amirzhan,<sup>1,4</sup> and Federico Capasso<sup>1</sup>

<sup>1</sup>*Harvard John A. Paulson School of Engineering and Applied Sciences,  
Harvard University, 29 Oxford Street, Cambridge, MA 02138*

<sup>2</sup>*Università Politecnica delle Marche, Via Brecce Bianche 60131, Ancona, Italy*

<sup>3</sup>*Applied Physics, Vrije Universiteit Brussel, Pleinlaan 2, 1050 Brussel, Belgium*

<sup>4</sup>*Department of Materials, Imperial College London, Prince Consort Rd, London SW7 2BP, UK*

Recently, it was shown that a Mie particle in an evanescent field ought to experience optical forces that depend on the helicity of the totally internally reflected beam. As yet, a direct measurement of such helicity-dependent forces has been elusive, as the widely differing force magnitudes in the three spatial dimensions place stringent demands on a measurement's sensitivity and range. In this study, we report the simultaneous measurement of all components of this polarization-dependent optical force by using a 3D force spectroscopy technique with femtonewton sensitivity. The vector force fields are compared quantitatively with our theoretical calculations as the polarization state of the incident light is varied and show excellent agreement. By plotting the 3D motion of the Mie particle in response to the switched force field, we offer visual evidence of the effect of spin momentum on the Poynting vector of an evanescent optical field.

It is well known that light carries momentum, so when it is absorbed or scattered by an intervening object, it exerts a force. These optical forces play an increasingly important role in the study of light momenta [1–5] and the manipulation of elements at the nano- and microscale [6–11]. Generally, the momentum density of light, sometimes known as the optical current [12], is proportional to its Poynting vector,  $\vec{p} \propto \text{Re} [\vec{E}^* \times \vec{H}]$ . Yet, recent theoretical studies, examining the generalized energy flow of light fields with spin angular momentum, have provided interesting examples where this is not the case [12, 14]. More specifically, the momentum density can be considered to have an *orbital* and a *spin* component,  $\vec{p} = \vec{p}_o + \vec{p}_s$ . The orbital momentum  $\vec{p}_o$ , usually referred to as the linear momentum, is proportional to the light field's phase gradient, while the spin momentum  $\vec{p}_s$  is proportional to the field's spin angular momentum.

The spin-momentum density  $\vec{p}_s$  was previously considered to be “virtual” because it exerts no force on a dipolar particle [12, 13, 15]. However, this quantity has found surprising relevance in the Mie regime, where scatterers are sized approximately the wavelength of light. For instance, a paraxial gaussian beam carrying spin angular momentum was shown to exhibit a vortex-shaped momentum flow in the plane perpendicular to its propagation, causing both orbital rotation and spin in an asymmetric probe particle [16]. In addition, the spin-momentum density of a tightly focused beam was indirectly probed by measuring a particle's asymmetric far-field scattering [17]. In 2013, it was shown that evanescent waves exhibit an extraordinary, helicity-dependent momentum, manifesting in a lateral force normal to the plane of incidence [3]. This unusual lateral force rapidly attracted both theoretical and experimental interest, and further work has uncovered many analogous phenomena in chiral particles and more complex field distributions [18–24]. A confirmation of the existence

of this lateral force was made in 2015 by observing a helicity-dependence in the total force acting on a nanocantilever [25].

However, a quantitative match between experiment and theory continued to be elusive. Such a measurement, to be unambiguous, must be made in the three dimensions simultaneously, using a probe whose geometry can be analytically modeled. This type of measurement is fundamentally challenging because the lateral force is between one and two orders of magnitude smaller than forces in the in-plane directions.

In this Letter, we introduce a floating-probe force spectroscopy technique with femtonewton resolution and piconewton range, capable of simultaneous measurement of a three-dimensional force field. The technique is uniquely suited to optical force measurements and can be tailored to generate a force map in a plane or a three dimensional volume. The instrument is pictured in Fig. 1.

A microsphere trapped in three dimensions by a tightly focused beam of light will experience a displacement due to an applied optical force [26]. For small perturbations relative to the particle's equilibrium position, its response may be modeled as an anisotropic, damped, harmonic oscillator [27]. Thus, for a general driving force,  $\tilde{x}_i(\omega) = \chi_{ij}(\omega)\tilde{F}_j(\omega)$ , where  $\tilde{F}_j$  is the complex force in the  $j$ -th spatial direction,  $\tilde{x}_i$  the complex displacement, and  $\chi_{ij}$  the frequency-dependent mechanical susceptibility function, where

$$(\chi^{-1}(\omega))_{ij} = \kappa_{ij} + i\omega\gamma_{ij}. \quad (1)$$

In our simplified model,  $\kappa_{ij}$ , the stiffness tensor describing the strength of the optical trap, and  $\gamma_{ij}$ , the directional drag coefficient, are assumed to have no off-diagonal elements. In other words, motions in the three spatial dimensions are treated as uncoupled. We perform a phase sensitive measurement of our probe's displacement in response to a periodically applied force against

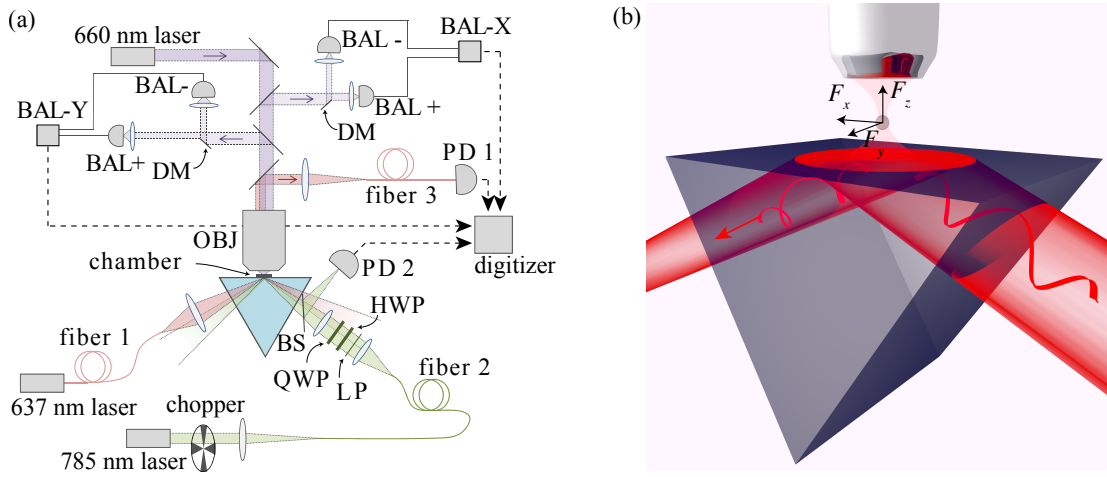


FIG. 1: Schematic depicting the *excitation and detection setup* in our experiment. (a) The *excitation* is provided by an evanescent wave. The continuous wave (CW) laser generating this field ( $\sim 100$  mW, 785 nm) is blocked periodically (10-100 Hz) by a chopper. A portion ( $\sim 5\%$ ) of the modulated light is picked off to form a *reference* signal for lock-in position measurement. The rest passes through, in order, a linear polarizer (LP), a half-wave plate (HWP), and a quarter-wave plate (QWP), which controls the polarization of the beam. Back-scattered light from the trap beam (660 nm CW) is used to determine the particle's  $x$  and  $y$  displacement in volts. BAL-X and BAL-Y are two balanced detectors whose positive and negative monitors are each fed half of the back-scattered light, as sectioned by two  $D$ -shaped mirrors (DM). The absolute separation  $z$  between the particle and the glass surface is determined by the light it scatters from a totally internally reflecting, 637 nm detection beam, maintained at around 1 mW power. In the schematic, PD1 tracks this signal in volts. (b) Detail showing the interaction of the trapped floating probe with the amplitude-modulated evanescent field, together with the coordinate system used to describe the forces acting on the particle.

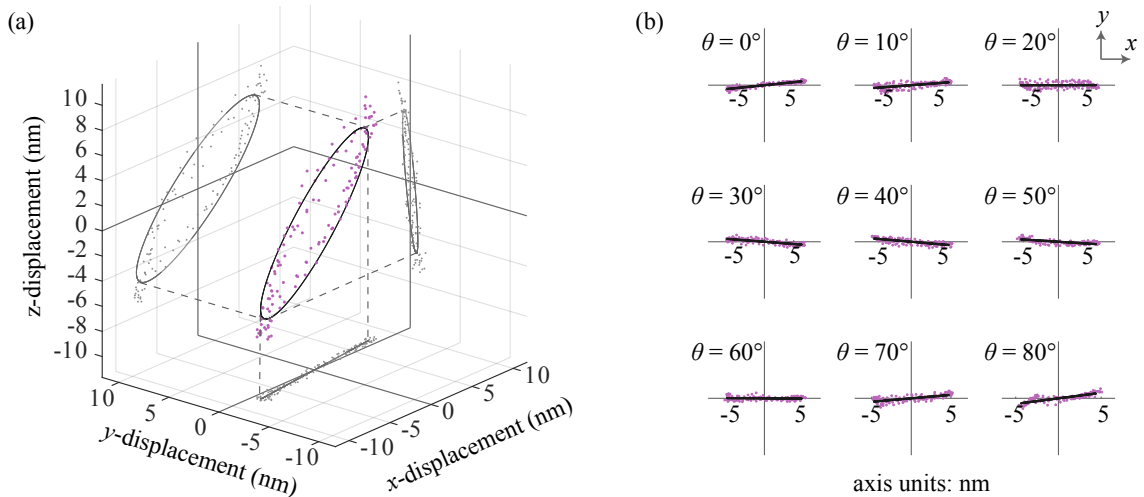


FIG. 2: Measured motion of the particle in response to a periodically, on-off modulated optical force. The particle, subject to an on-off optical force modulated in amplitude by a chopper set at 50 Hz, traces an ellipse in three dimensions due to the anisotropy of the mechanical response. The response is cyclical with a period matching the square-wave fundamental frequency. (a) For a single force measurement of 100 s duration, a particle's average trajectory in 3D space, along with its projection onto each orthogonal plane is plotted. Here the HWP angle was set to  $0^\circ$ . (b) The projection of a particle's measured motion in the  $(x, y)$ -plane as a half-wave plate is rotated between  $0^\circ$  and  $80^\circ$ , in steps of  $10^\circ$ . Due to the mechanical system's high degree of spatial symmetry in the  $(x, y)$ -plane, the particle's motion is roughly aligned with the vector direction of the in-plane optical force. The effect of the optical field's spin momentum on the particle motion is evident here as a change in tilt of the particle's projected trajectory in the  $(x, y)$ -plane as the evanescent field's helicity is changed. The maximum displacement measured in the  $y$ -direction is around 0.5 nm.

a large thermal noise background [26]. Total variance in particle position is a function only of the trap spring constant,  $\kappa$ , and the thermal energy,  $k_B T$  ( $\sigma_x = \sqrt{\frac{k_B T}{\kappa}}$ ). However, the signal to noise ratio (SNR) of a band-

limited measurement of the probe position is independent of  $\kappa$ , a function of only temperature, drag, bandwidth  $\Delta f$ , and magnitude of the applied force  $F_0$ :

$$\text{SNR} = F_0 / \sqrt{4\gamma k_B T \Delta f}, \quad (2)$$

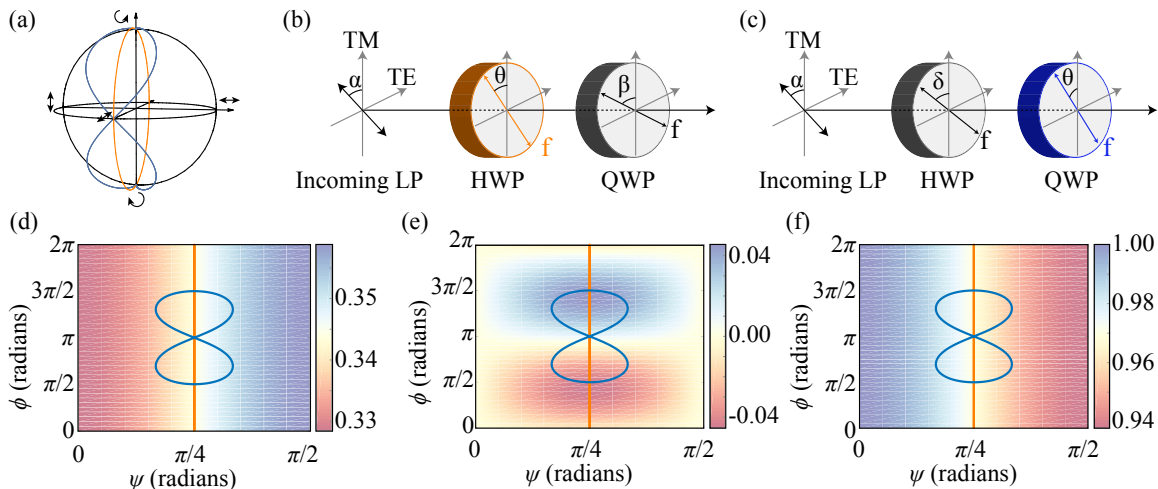


FIG. 3: **Theoretical prediction of net force on a Mie particle as a function of the polarization state of an evanescent beam.** (a) The polarization traces take two different closed paths, orange line and blue line on the Poincaré sphere, depending on whether the half-wave plate or quarter-wave plate is rotated, respectively. (b) The incident linearly polarized light, from the fiber, forms an angle  $\alpha = 40^\circ$  with the vertical (TM) axis. The half-wave plate is rotated by angle  $\theta$  from  $0^\circ$  to  $180^\circ$ , while the quarter-wave plate is fixed at  $\beta = 45^\circ$ . (c) Alternate path where the half-wave plate is fixed at  $\delta = 42.5^\circ$  and the quarter-wave plate is rotated by angle  $\theta$  from  $0^\circ$  to  $180^\circ$ . It is important to note that  $\alpha$ ,  $\beta$ , and  $\delta$  are fixed angles with different values.  $\theta$  is the angle that is varied during a trace. In (b)-(c) the light is propagating from left to right ( $f$  denotes the fast axis of the waveplates). (d)-(f) Mie theory prediction for the evanescent optical force spatial components  $F_x$ ,  $F_y$ , and  $F_z$ , respectively, as defined in Fig. 1(b), with parametrized paths shown superimposed (blue for QWP and orange for HWP). The forces are normalized to the largest force (i.e.,  $\max F_z$ ).

where the denominator is the RMS contribution of the stochastic thermal force (SM). Importantly, the SNR is also independent of frequency, affording us the necessary freedom to conduct our measurements at a central frequency of our choosing. The trapped particle’s periodic response to the optical driving force has an amplitude and relative phase determined by the particle’s mechanical susceptibility, as defined in Eq. (1). In the presence of mechanical anisotropy, the trajectory generally takes on the form of a tilted ellipse in 3D space [28]. Fig. 2 shows such a trajectory, along with its projections onto the three orthogonal planes. From the particle’s complex response (in amplitude and phase) in each dimension, a real force can be extracted if the particle’s mechanical susceptibility is known.

An evanescent wave generated by a beam with nonzero helicity carries both longitudinal momentum in the direction of propagation ( $x$ ) as well as spin momentum perpendicular to the plane of incidence ( $y$ ). Depending on the properties of the scatterer, the interaction with these momenta will generate different types of forces. An in-plane ( $x - z$ ) scattering force results from the transfer of longitudinal momentum in the Mie scattering process. This force is orders of magnitude larger than any possible out-of-plane ( $y$ ) lateral force which depends on the helicity of the incident light [29].

Through the combination of a half-wave plate (HWP) and a quarter-wave plate (QWP), any pure polarization state of a light beam can be accessed. A continuous change in polarization traces a path on the surface of

the Poincaré sphere. As Fig. 3 shows, a rotation of the HWP through  $90^\circ$  with the QWP fixed at  $45^\circ$  traces a great circle on the Poincaré sphere while a rotation of the QWP through  $180^\circ$  draws a figure-eight. Both described trajectories pass through the north and south poles of the sphere, corresponding to the right and left circular polarizations of light, respectively.

The optical force fields derived by an exact, analytical Mie scattering calculation assuming a  $1 \mu\text{m}$  diameter polystyrene (PS) sphere with index  $n = 1.58$  and negligible absorption are shown in Fig. 3(d-f) as a function of two independent polarization parameters  $\psi$  and  $\phi$ , which define the polarization state of the incident field  $\vec{E}$ :

$$\vec{E} \propto \sin \psi \hat{e}_{TE} + e^{i\phi} \cos \psi \hat{e}_{TM}, \quad (3)$$

where the  $\hat{e}_{TM}$  and  $\hat{e}_{TE}$  unit vectors point in the TM and TE polarization directions of a linearly polarized totally internally reflecting beam.  $\hat{e}_{TE}$  is the same as  $\hat{y}$  in our coordinate system.  $\psi$ ,  $\phi$  can be parametrized by the HWP and QWP rotation angles (SM). We note that while  $F_x$ , the force along the evanescent field’s direction of propagation, and  $F_z$ , the force perpendicular to the surface, are expected to depend only on  $\psi$ , the “lateral force”,  $F_y$ , is sensitive to changes in helicity, or  $\phi$ .

After calibration procedures (described in SM [30]) which determine the system mechanical parameters as functions of height ( $z$ ), the bead is held in a constant position, usually a few hundred nanometers from the surface, maintained by several feedback control loops, while the polarization state of the excitation beam is changed.

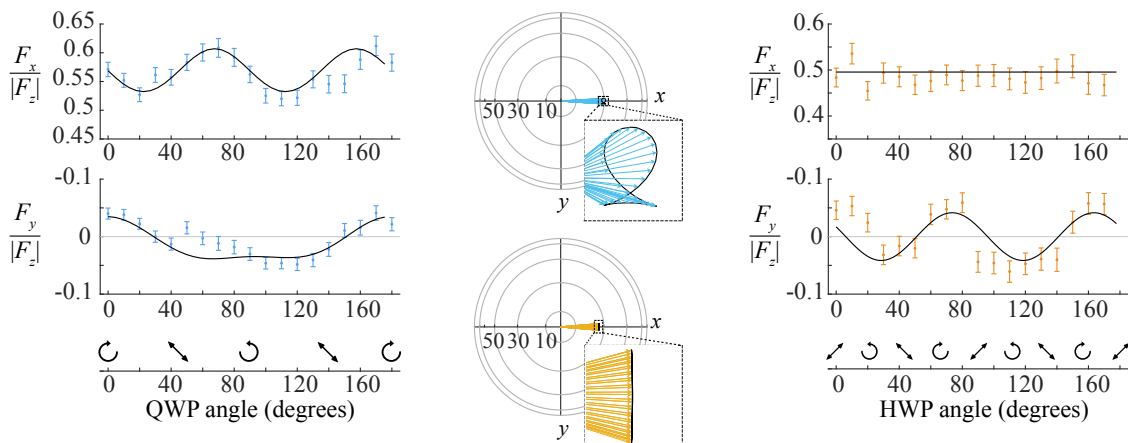


**FIG. 4: Measured optical forces on two polystyrene spheres.**  $F_x/|F_z|$  and  $F_y/|F_z|$ , the measured, normalized, optical forces, are compared against their analytical predictions (black). The modulation frequency for the lock-in detection is 50 Hz. Although the waveplate is mounted on a rotary mount, marked in  $2^\circ$  increments, its manual rotation by hand introduces some additional uncertainty in the angle of rotation. (Left) The light beam's polarization state is changed along the blue line in Fig. 3, by rotating the quarter-wave plate from 0 to 180 degrees. The particle has a measured radius of  $1.4 \mu\text{m}$ , its average height is  $400 \text{ nm}$  from the chamber surface, and the beam's angle of incidence is  $63^\circ$  from normal. The average measured value for  $F_z$  is  $257 \text{ fN}$  towards the surface. The black curve showing the analytical prediction for  $F_x/|F_z|$  has been scaled by a factor of 0.9 to fit our data; the bottom curve is not scaled. (Right) The light beam's polarization state is changed along the orange line in Fig. 3, by rotating the half-wave plate from 0 to 180 degrees. This corresponds to two full traces of the great circle of the Poincaré sphere. The particle has a measured radius of  $1.3 \mu\text{m}$ , its average height is  $260 \text{ nm}$ , and the beam's angle is the same at  $63^\circ$ . Average  $F_z$  is  $155 \text{ fN}$  towards the surface. The top curve is scaled by 0.86 to fit our data; the bottom curve is not scaled. (Center) Projection view shows the angular variation of the net force as the QWP (blue) and HWP (orange) are rotated. Maximum angular change is around  $7^\circ$  for the QWP and  $9^\circ$  for the HWP. Line of sight is along the  $+z$  direction.

Each data point is 100 s of integration, and simultaneously determines all three components of the optical force,  $\vec{F}$ , with femtonewton resolution. Both 18-point sweeps reported in Fig. 4 were obtained in a total of 30 minutes. Forces are normalized by  $|F_z|$ , the magnitude of the force in the vertical direction, allowing our measurements to be independent of excitation laser intensity. Plotted errors reflect RMS thermal noise, found to be around 3 fN in the lateral directions ( $F_x, F_y$ ) and 5 fN in the vertical ( $F_z$ ). While the average attractive  $|F_z|$  in these two sweeps was 257 fN and 155 fN for the QWP and HWP measurements, respectively, the maximum force in the lateral,  $y$ -direction was only around 10 fN and 7 fN: a ratio of 25 to 1. These forces correspond to lateral displacements of around 0.5 nm and 0.3 nm, respectively. From the ratios of the three components of the optical force, we can build a vector plot displaying the orientation of the net force in space. In the center panel of Fig. 4, we plot on a unit sphere the direction of the net force as QWP and HWP angles are changed. The view is along the  $+z$  direction—from below the particle. The inset shows in more detail the path of angular variation. The maximum change in angle is about  $7^\circ$  for the QWP and  $9^\circ$  for the HWP.

Agreement with theory is within 10%, with the largest systematic error contributed by uncertainty in particle radius, which is deduced from least-squares fits to hindered diffusion theory [33, 34]. The fit is sensitive to uncertainties in measured particle-surface separations. Ad-

ditionally, misalignment of our detection and excitation coordinate systems, as well as a slight coupling between nominally independent directions of motion, cannot be completely avoided. This coupling is considered in detail in SM [30].

Given the overall close agreement with theory, and the compelling visual evidence of spin-momentum's effect on the measured direction of net optical force, we feel confident to report that we have made the first three-dimensional, quantitative measurement of the helicity-dependent spin-momentum force acting on a Mie particle, representing a significant step forward in the systematic study of these and other exotic optical forces. In doing so, we developed a novel method to map a particle's 3D interaction with an optical field with volume scanning capabilities, piconewton dynamic range and femtonewton force resolution.

We acknowledge the support of NSF GFRP grant number DGE1144152 and the Research Foundation Flanders grant number 12O9115N. All fabrication was done in the Harvard Center for Nanoscale Sciences (CNS) clean room facility. We kindly thank the groups of Evelyn Hu and David Weitz at Harvard University for shared equipment and lab access. We thank Paul Mehaignerie for his assistance with Fig. 3, Michail Schwab for visualization ideas.

\* [ginis@seas.harvard.edu](mailto:ginis@seas.harvard.edu)

- [1] M. Padgett and R. Bowman, *Nat. Photonics* **5**, 343-348, (2011).
- [2] K. Y. Bliokh, A. Y. Bekshaev, and F. Nori, *New J. Phys.* **15**, 033026, (2013).
- [3] K. Y. Bliokh, A. Y. Bekshaev, and F. Nori, *Nat. Commun.* **5**, 3300, (2014).
- [4] A. Aiello, P. Banzer, M. Neugebauer, and G. Leuchs, *Nat. Photon.* **9**, 789-795, (2015).
- [5] K. Y. Bliokh and F. Nori, *Phys. Rep.* **592**, 1-38, (2015).
- [6] D. G. Grier, *Nature* **424**, 810-816, (2003).
- [7] G. Anetsberger, O. Arcizet, Q. P. Unterreithmeier, R. Riviere, A. Schliesser, E. M. Weig, J. P. Kotthaus, and T. J. Kippenberg, *Nat. Phys.* **5**, 909-914, (2009).
- [8] M. L. Juan, R. Gordon, Y. Pang, F. Eftekhari, and R. Quidant, *Nat. Phys.* **5**, 915-919, (2009).
- [9] T. Li, S. Kheifets, and M. G. Raizen, *Nat. Phys.* **7**, 527-530, (2011).
- [10] O. M. Maragò, P. H. Jones, P. G. Gucciardi, G. Volpe, and A. C. Ferrari, *Nat. Nanotech.* **8**, 807-819, (2013).
- [11] M. L. Juan, C. Bradac, B. Besga, M. Johnsson, G. Brennen, G. Molina-Terriza, and T. Volz, *Nat. Phys.* **13**, 241-245, (2017).
- [12] M. V. Berry, *J. Opt. A-Pure Appl. Op.* **11**, 094001, (2009).
- [13] F. J. Belinfante, *Physica* **7**, 449-474, (1940).
- [14] A. Y. Bekshaev and M. Soskin, *Opt. Commun.* **271**, 332-348, (2007).
- [15] P. Chaumet and M. Nieto-Vesperinas, *Opt. Lett.* **25**, 1065-1067, (2000).
- [16] O. Angelsky, A. Y. Bekshaev, P. Maksimyak, A. Maksimyak, S. G. Hanson, and C. Y. Zenkova, *Opt. Express* **20**, 3563-3571, (2012).
- [17] M. Neugebauer, T. Bauer, A. Aiello, and P. Banzer, *Phys. Rev. Lett.* **114**, 063901, (2015).
- [18] S. Wang and C. Chan, *Nat. Commun.* **5**, 3307, (2014).
- [19] F. J. Rodríguez-Fortuño, N. Engheta, A. Martínez, and A. V. Zayats, *Nat. Commun.* **6**, 8799, (2015).
- [20] A. Y. Bekshaev, K. Y. Bliokh, and F. Nori, *Phys. Rev. X* **5**, 011039, (2015).
- [21] A. Hayat, J. B. Mueller, and F. Capasso, *Proc. Natl. Acad. Sci. U.S.A.* **112**, 13190-13194, (2015).
- [22] M. Alizadeh and B. M. Reinhard, *Opt. Express* **24**, 8471-8479, (2016).
- [23] H. Chen, C. Liang, S. Liu, and Z. Lin, *Phys. Rev. A* **93**, 053833, (2016).
- [24] T. Zhang, M. R. C. Mahdy, Y. Liu, J. H. Teng, C. T. Lim, Z. Wang, and C.-W. Qiu, *ACS Nano* **11**, 4292-4300, (2017).
- [25] M. Antognozzi, C. R. Bermingham, R. L. Harniman, S. Simpson, J. Senior, R. Hayward, H. Hoerber, M. R. Dennis, A. Y. Bekshaev, K. Y. Bliokh, and F. Nori, *Nat. Phys.* **12**, 731-735, (2016).
- [26] L. Liu, S. Kheifets, V. Ginis, and F. Capasso, *Phys. Rev. Lett.* **116**, 228001, (2016).
- [27] G. E. Uhlenbeck and L. S. Ornstein, *Phys. Rev.* **36**, 823-841, (1930).
- [28] L. Liu, S. Kheifets, V. Ginis, A. Di Donato, and F. Capasso, *Proc. Natl. Acad. Sci. U.S.A.* **114**, 11087-11091, (2017).
- [29] S. Albaladejo, M. I. Marqués, M. Laroche, and J. J. Sáenz, *Phys. Rev. Lett.* **102**, 113602, (2009).
- [30] See Supplemental Material [url], which includes Refs. [31-32], for detailed descriptions of the experimental setup, the data analysis, the alignment procedures, and the numerical force simulations.
- [31] L. Liu, A. Woolf, A. W. Rodriguez, and F. Capasso, *Proc. Natl. Acad. Sci. U.S.A.* **111**, E5609 (2014),
- [32] E. Almaas and I. Brevik, *Journal of the Optical Society of America B* **12**, 2429 (1995).
- [33] H. Brenner, *Chem. Eng. Sci.* **16**, 242-251, (1961).
- [34] A. Goldman, R. G. Cox, and H. Brenner, *Chem. Eng. Sci.* **22**, 637-651, (1967).